QUANTUM PROCESSING

Error-detected quantum operations with neutral atoms mediated by an optical cavity

Brandon Grinkemeyer[1]†, Elmer Guardado-Sanchez[1]†, Ivana Dimitrova[1]†, Danilo Shchepanovich[1], G. Eirini Mandopoulou[1], Johannes Borregaard[1], Vladan Vuletić[2,3], Mikhail D. Lukin[1]*

Neutral-atom quantum processors are a promising platform for large-scale quantum computing. Integrating them with optical cavities enables fast nondestructive qubit readout and access to fast remote entanglement generation for quantum networking. In this work, we introduce a platform for coupling single atoms in optical tweezers to a Fabry-Perot fiber cavity. Leveraging the strong atom-cavity coupling, we demonstrated fast qubit-state readout with 99.960^{+14}_{-24}% fidelity and two methods for cavity-mediated entanglement generation with integrated error detection. First, we used cavity-carving to generate a Bell state with 91(4)% fidelity and a 32(1)% success rate (the number in parentheses is the standard deviation). Second, we performed a cavity-mediated gate with a deterministic entanglement fidelity of 52.5(18)%, increased to 76(2)% with error detection. Our approach provides a route toward modular quantum computing and networking.

Neutral-atom arrays are a promising platform for large-scale quantum information systems, enabling quantum algorithms with multiple logical qubits (*1*) and new approaches to quantum metrology and clocks (*2*–*5*). These advancements have been facilitated by the implementation of high-fidelity two-qubit gates and the use of coherent transport for nonlocal connectivity and reconfigurable architecture (*6*–*9*). Although quantum processors with more than 10,000 physical qubits appear within the reach (*10*), further scaling may benefit from a modular approach, in which quantum computation is distributed across quantum processors connected by fast high-fidelity quantum network channels (*11*–*16*). Such an approach requires integration of atom arrays with optical cavities, which provides direct coupling to photons in an optical mode that can be easily collected for fast high-fidelity remote entanglement distribution (*17*, *18*). Integration of individually controlled atoms in optical tweezers with an optical cavity has only recently been realized experimentally (*19*–*22*).

In this work, we demonstrated a platform that combines individual control and transport of atoms in optical tweezers with efficient coupling to individual optical photons enabled by a Fabry-Perot fiber cavity (FPFC). These cavities offer large cooperativities ($C \sim 100$) (*23*, *24*) while also providing optical access for optical tweezers. This approach can be directly integrated with a reconfigurable architecture in which a neutral-atom array is placed above the cavity and select atoms are coherently transported in and out of the cavity mode (*14*, *19*). This further enhances the capabilities of a neutral-atom quantum computer, enabling an efficient distributed processor. We carried out several experiments to demonstrate the capabilities of this platform. Specifically, we demonstrated that the high cooperativity enables a fast high-fidelity qubit-state readout, which can be important for accelerating quantum error-correction algorithms. Moreover, we have shown that error detection can be naturally integrated within this approach to enable robust entanglement generation. Unlike previous demonstrations of cavity-mediated entanglement that relied on photon detection, our protocol heralds success based on the atomic state, which increases the success rate of entanglement generation, improving the efficiency of a quantum networking scheme that relies on probabilistic Bell measurements (*25*). This method can be used for fast and more complex quantum network operations such as entanglement swapping, purification, and fusion, which can enable the development of an efficient distributed quantum computer (*26*–*28*).

Atom-cavity platform

We coupled individually controlled rubidium-87 atoms trapped in optical tweezers to a FPFC. These microcavities exhibit low scattering loss and small radii of curvature, which allow for a small mode volume and high cooperativity (*23*). Our FPFC design features mirror diameters of 125 μm and a cavity length of 100 μm, providing ample optical access for single atoms in optical tweezers [(*29*), section 1]. We loaded atoms into optical tweezers from a magneto-optical trap (MOT) formed directly above the FPFC. The atoms were then transported ~60 μm into the cavity mode and deposited into an optical lattice formed by an 850-nm cavity mode (Fig. 1A). The atoms were positioned in the 850-nm mode to maximize their overlap with the 780-nm mode, as described in (*29*), section 2.2. The FPFC was stabilized by using an 810-nm laser referenced to an external ultralow expansion (ULE) cavity, ensuring that the 780-nm cavity mode remained locked to the $|5S_{1/2}\rangle \leftrightarrow |5P_{3/2}\rangle$ $D2$ transition of rubidium-87. Additionally, the cavity resonance can be dynamically tuned across the entire hyperfine structure during an experimental sequence, (Fig. 1B) [(*29*), section 2.4]. The atom-cavity system was characterized by probing the transmission spectrum of the cavity through the single-mode input port by using circularly polarized (σ^+) light. By pumping the atoms to the stretched state $|F = 2, m_F = 2\rangle$ with the cavity resonant to the $F = 2 \leftrightarrow F' = 3'$ transition, we realized an effective two-level system. The excitation spectrum of a single atom showcased a strong resolvable vacuum-Rabi splitting, showing the hybridization of the atomic and photonic excitations (Fig. 1C). Fitting the transmission spectrum to an analytical model [(*29*), section 4.1], we extracted an atom-photon coupling strength of $g = 2\pi \times 100.0(8)$ MHz and cavity linewidth (full width at half maximum) of $\kappa = 2\pi \times 65(1)$ MHz (where the numbers in parentheses are the standard deviation). This results in a single-atom cooperativity of $C = \frac{4g^2}{\kappa\Gamma} = 101(2)$, where $\Gamma = 2\pi \times 6$ MHz is the natural linewidth of the excited state.

When probed on resonance, the difference in transmission between an atom coupled and no atom coupled to the cavity allows for fast nondestructive readout by thresholding transmitted photon counts (*24*, *30*–*32*). Through this measurement, atom presence could be detected with a fidelity of 99.988^{+7}_{-23}% in 10 μs and of 99.950^{+24}_{-49}% in 2.5 μs, limited by the finite atom lifetime [(*29*), section 3.2.1]. Additionally, this readout is nearly lossless, with a measured loss of 0.034^{+27}_{-6}%. In all of our experiments, we postselected on atomic presence at the end of the experimental sequence [(*29*), section 2]. Furthermore, this measurement can differentiate atoms in the qubit manifold, which we encoded in the magnetic-field insensitive states: $|0\rangle = |F = 1, m_F = 0\rangle$ and $|1\rangle = |F = 2, m_F = 0\rangle$. During readout, the cavity was tuned to the $2 \leftrightarrow 3'$ transition, so that the $|1\rangle$ state was coupled to the cavity, whereas the $|0\rangle$ state was not. Using the state-dependent coupling, we performed fast nondestructive readout of the qubit state with fidelity of 99.960^{+14}_{-24}% in 10 μs, limited by off-resonant scattering from the 850-nm trap and state preparation. For state readout, we collected 0.09(2) photons from the $F = 2$ state and 16.600(1) photons from the $F = 1$ state (Fig. 1D). Increasing the cooperativity of the cavity would allow for faster readout and as a result higher readout fidelities

[1]Department of Physics, Harvard University, Cambridge, MA, USA. [2]Department of Physics, Massachusetts Institute of Technology, Cambridge, MA, USA. [3]Research Laboratory of Electronics, Massachusetts Institute of Technology, Cambridge, MA, USA.
*Corresponding author. Email: lukin@physics.harvard.edu
†These authors contributed equally to this work.

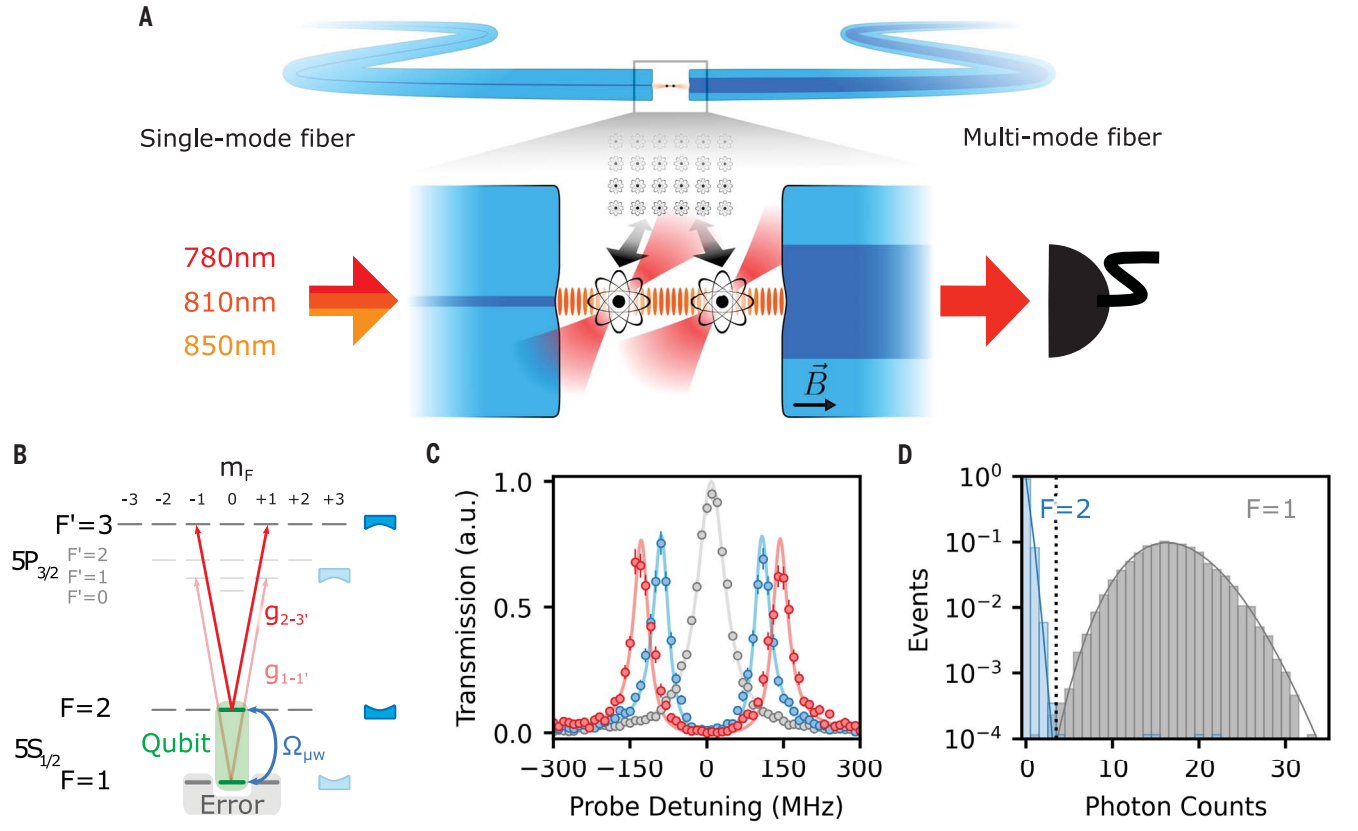

Fig. 1. Experimental setup and qubit readout. (**A**) Atoms in optical tweezers were loaded above a FPFC and transported into the cavity mode. The FPFC has a single-mode input port and a multimode output port, over which we collected transmitted light. The FPFC length was stabilized by using an 810-nm laser, and the atoms were trapped in a 850-nm mode of the cavity. The 780-nm mode coupled to the D2 line in rubidium. The magnetic field was aligned along the cavity axis. (**B**) Atomic-level diagram of rubidium-87. Readout was performed with the cavity on resonance with the 2 ↔ 3′ transition, whereas for entanglement generation the cavity was tuned to the 1 ↔ 1′ transition. (**C**) Resonant transmission spectra of a bare cavity (gray), one atom (blue), and two atoms (red) coupled to the cavity. The lines are a simultaneous fit, yielding parameters $g = 2\pi \times 100.0(8)$ MHz and $\kappa = 2\pi \times 65(1)$ MHz, resulting in a cooperativity of $C = 101(2)$. (**D**) Histograms showing photon counts collected in 10 μs with an atom in the $F = 1$ state (gray) and an atom in the $F = 2$ state (blue), yielding a qubit-state readout fidelity of 99.960^{+14}_{-24}%.

[(*29*), section 3]. Readout left the $|0\rangle$ state undisturbed, whereas it quickly pumped the $|1\rangle$ state to the stretched $|F = 2, m_F = 2\rangle$ state. In principle, a Raman pulse can be used afterward to reinitialize the atom in $|1\rangle$, making this readout nondestructive to the qubit state [(*29*), section 3.3].

Photon-mediated entanglement through dark states

We realized quantum entanglement between two atoms coupled to a cavity by use of a photonic dark state. This state is an antisymmetric superposition in which one atom is excited out of phase with the other, leading to destructive interference in the cavity mode, rendering it dark to the cavity. Although such states have been studied previously (*20*, *33*), their potential for quantum operations remains largely unexplored.

Specifically, we probed the system by exciting both atoms from the side, rather than through the single-mode input port, and measured the same signal: the light transmitted through the multimode optical fiber. We varied both the cavity detuning Δ_C and the probe detuning Δ_P. With a single atom coupled to the cavity, we directly observed an avoided crossing in the energy levels, similar to what is shown in Fig. 1C. Moreover, the dressed states became more atom-like close to the atomic resonance and more cavity-like close to the cavity resonance, resulting in stronger and weaker coupling to the side beam drive, respectively (Fig. 2A). With two atoms coupled to the cavity, similar behavior was observed but with an expected $\sqrt{2}$ enhancement of the splitting (Fig. 2B). These two features correspond to the "bright states," given by $|B_\pm\rangle = \frac{1}{2}(|eg,0\rangle + |ge,0\rangle) \pm \frac{1}{\sqrt{2}}|gg,1\rangle$. In contrast to the spectrum recorded when the cavity mode was excited through the fiber, an additional third feature appeared at the atomic resonance that we attribute to a photonic dark state, $|D_0\rangle = \frac{1}{\sqrt{2}}(|eg,0\rangle - |ge,0\rangle)$ (Fig. 2C), where $|g\rangle$ and $|e\rangle$ are the atomic ground and excited states of each atom, respectively, and the number indicates the number of photons in the cavity. Because of the lack of a photonic component, this state can only be driven by exciting the atom and not the cavity. Specifically, for a global drive, a relative phase of π between the drive on the two atoms is required. Because of thermal motion of the atoms, the relative phase between the two atoms and the drive beam changed from shot to shot, and we consistently observed the dark state as a bright feature. Furthermore, a strong drive allows for excitation of the cavity through the dark state. In the rest of our experiments, we individually drove single atoms, which maintained a coupling to both dark and bright states, while being insensitive to the relative phase between the atoms [(*29*), section 4].

To use this dark state to implement cavity-mediated entanglement between the two atoms, when the cavity is resonant with the bare atomic transition the difference between the single- and two-atom spectra can

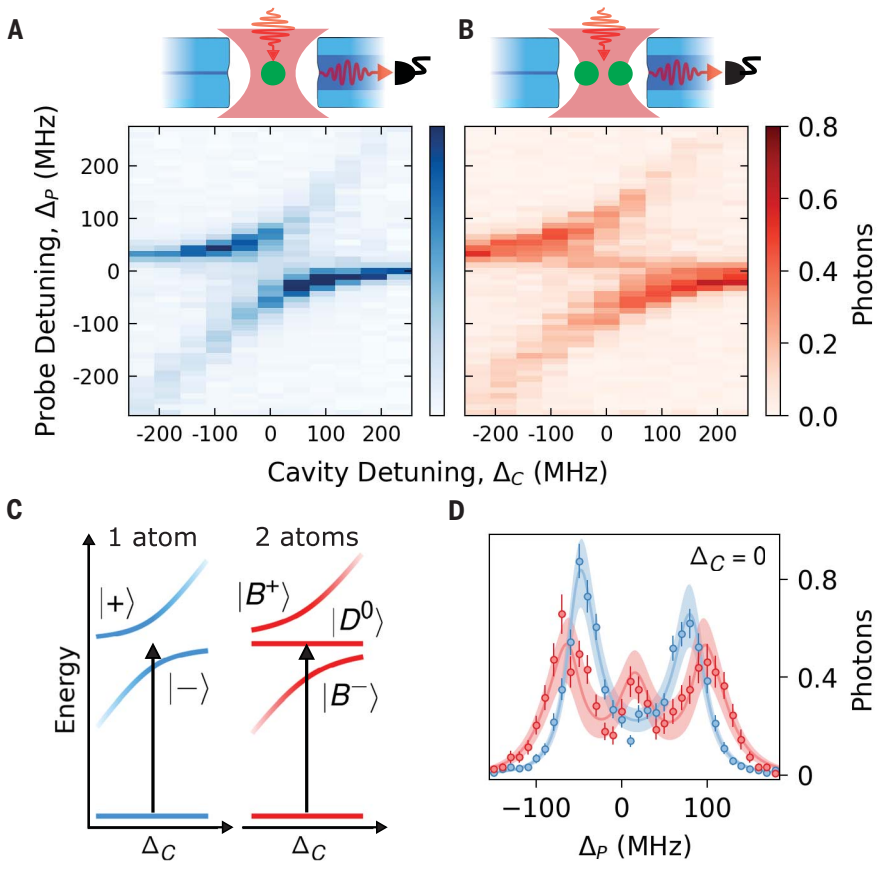

Fig. 2. Photonic dark state spectroscopy. (**A** and **B**) Side drive spectroscopy of (A) one and (B) two atoms coupled to the cavity as a function of cavity and probe laser detuning (Δ_C and Δ_P, respectively). With two atoms coupled to the cavity, the spectrum reveals a feature on resonance with the atomic transition, corresponding to a photonic dark state. (**C**) Energy level diagram of the first excitation manifold for one and two atoms coupled to a single cavity mode, which correspond to the states probed in the spectra plotted against the cavity detuning, Δ_C [(*29*), section 4.1]. (**D**) Probe spectroscopy at $\Delta_C = \Delta_A$ for one (blue circles) and two (red circles) atoms coupled to the cavity while probed with a side beam. Lines are simultaneous fits to a numerical model [(*29*), section 4.2].

be interpreted as a conditional resonance. The system can only be excited with a resonant beam if both atoms are coupled to the cavity (Fig. 2D). By encoding the $|0\rangle$ and $|1\rangle$ qubit states so that one was coupled to the cavity and the other was uncoupled, the conditional resonance became state dependent, enabling two-qubit quantum operations. However, the fidelity of these operations was limited by errors arising from photon leakage out of the cavity and scattering into free space. We could improve this fidelity by engineering these leakage and scattering events to leave the atom in a specific state, $|err\rangle$, outside the qubit manifold. Through sequences of readout, π-pulses, and local optical pumping, we could measure the qubit states $|0\rangle$ and $|1\rangle$, as well as $|err\rangle$ [(*29*), section 3.3]. By postselecting on cases in which no error occurred, the fidelity will ultimately be limited by the presence of undetectable errors (*34*, *35*).

For entanglement experiments, we used the excited state $|e\rangle = |F' = 1, m_F = 0\rangle$, which has branching ratios that result in decay predominantly to the $|err\rangle = |F = 1, m_F = \pm 1\rangle$ states, whereas selection rules forbid decay to the $|0\rangle$ state (Fig. 3A). We performed a local drive on one of the atoms, which we call atom A, resonant with the $2 \leftrightarrow 1'$ transition. This drive couples $|1\rangle_A$ to $|e\rangle_A$. We shifted the cavity resonance to the $1 \leftrightarrow 1'$ transition so that it coupled $|err\rangle_A \leftrightarrow |e\rangle_A$ and $|0\rangle_B \leftrightarrow |e'\rangle_B$, where $|e'\rangle = |F' = 1, M_F = \pm 1\rangle$ state. As a result, the two-qubit state $|1\rangle_A|1\rangle_B \equiv |11\rangle$ acts as a single atom coupled to the cavity and experiences a suppressed excitation. By contrast, the $|10\rangle$ state behaves as two atoms coupled to the cavity and experiences a resonant coupling to the photonic dark state, $|D_0\rangle = 1/\sqrt{2}\left(|err\rangle_A|e'\rangle_B - |e\rangle_A|0\rangle_B\right)$ [(*29*), section 6]. This establishes a qubit state–dependent resonance, which is necessary to perform quantum operations between the two qubits.

Our first protocol relies on the state-dependent decay of the two-qubit states. This decay mechanism enables us to selectively remove, or "carve out," specific parts of the wave function, leaving behind the desired quantum state. Under a weak drive, we observed that the $|11\rangle$ and $|10\rangle$ states both decay into the $|err\rangle_A$ state with different rates. The resonant coupling to the dark state makes the $|10\rangle$ state rapidly decay, whereas the $|11\rangle$ experiences a suppressed decay (Fig. 3B). This allowed us to "carve out" the $|10\rangle$ state from the wave function (*19*, *35*, *36*). To prepare an entangled state with this mechanism, we first prepared an equal superposition of all two-qubit states, followed by the application of a drive pulse that carves out the $|10\rangle$ component. A global π-pulse flips the two-qubit state, and a second carving pulse once again carves out the $|10\rangle$ component. This sequence prepares a statistical mixture of error states and a Bell state: $\rho = |\Phi^-\rangle\langle\Phi^-| + |err\rangle_A\langle err|$. By postselecting on the atoms not being in the error state, we are left with the maximally entangled state, $|\Phi^-\rangle = \frac{1}{\sqrt{2}}(|00\rangle - |11\rangle)$. In principle, the minimal application of our scheme would be the spin-echo sequence described above: $\frac{\pi}{2} - \tau - \pi - \tau - \frac{\pi}{2}$. In practice, we found that the spin-echo scheme was limited owing to a coherent linear phase accumulation in the $|11\rangle$ state during the carving pulses that we attribute to laser phase noise [(*29*), section 6]. To cancel this linear phase, we implemented a Carr-Purcell decoupling sequence of the form $\frac{\pi}{2} - \frac{\tau}{2} - \pi - \tau - \pi - \frac{\tau}{2} - \frac{\pi}{2}$. We show in Fig. 3C the measured correlations in the *ZZ*, *XX*, and *YY* basis, resulting in a Bell state fidelity of $\mathcal{F} = 91(4)\%$ and a success probability of 32(1)%.

The theoretical limit on fidelity is set by undetectable errors—when a scattering event leaves the atoms in the qubit manifold instead of in the error state. The dominant source of undetectable errors arose from scattering from the dark state, which could decay through atom A or through atom B with equal probability. Decay through atom B left atom A in the state $|err\rangle_A$, so that this decay was fully detectable. Decay through atom A resulted in 17% undetectable errors for a single atom given by Clebsch-Gordon coefficients and owing to our current readout sequence, which cannot distinguish the $F = 2$ Zeeman sublevels. This led to total-dark-state scattering errors being 91.5% detectable. With this, we found a maximum theoretical fidelity of ~96.3% for our carving protocol. As predicted by our model, the entanglement fidelity increased exponentially but was still limited by unwanted scattering (Fig. 3D), which we attribute to level-mixing of the excited states from our traps and to imperfect polarization. Increasing the cooperativity would enhance the success

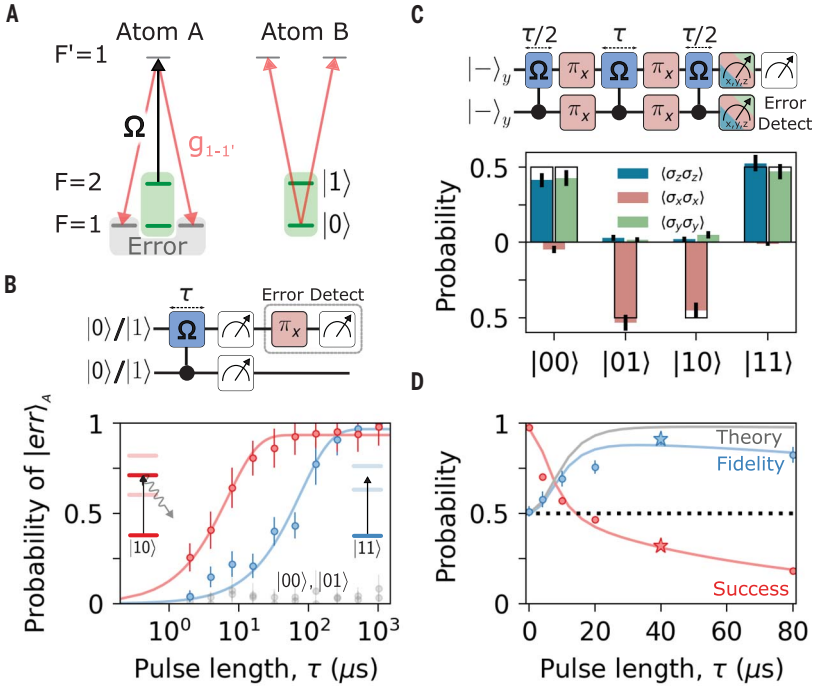

Fig. 3. Bell state preparation with cavity carving. (**A**) For entanglement generation, the cavity is tuned to the $1 \leftrightarrow 1'$ transition, and a single side drive on the $2 \leftrightarrow 1'$ transition is applied to atom A only. (**B**) (Top) Quantum circuit for preparing two-qubit states and measuring the $|err\rangle_A$ population. (Bottom) Decay rates into the error states after preparing each of the four two-qubit states. The resonant coupling to the dark state $|D_0\rangle$ results in much faster decay of $|10\rangle$ compared with the off-resonant coupling in $|11\rangle$. $|00\rangle$ and $|01\rangle$ do not couple to the driving beam. (**C**) (Top) Quantum circuit of a Carr-Purcell cavity-carving scheme, which prepares a $|\Phi^-\rangle$ Bell state. (Bottom) Measured correlations in the *ZZ* (blue), *XX* (red), and *YY* (green) bases verify that $|\Phi^-\rangle$ is prepared with a Bell state fidelity of $\mathcal{F} = 91(4)\%$ and a success probability of 32(1)%. Direction of the histograms indicate the expected sign of parity for $|\Phi^-\rangle$ in each bases. (**D**) Bell state fidelity (blue circles) and success probability (red circles) as a function of carving pulse length τ. Stars indicate the data presented in (C). Lines are a fit to a semiclassical numerical model, and the gray line is the expected Bell state fidelity without state-preparation and measurement errors [(*29*), section 7.1]. The dotted line indicates the fidelity limit for verifiable entanglement.

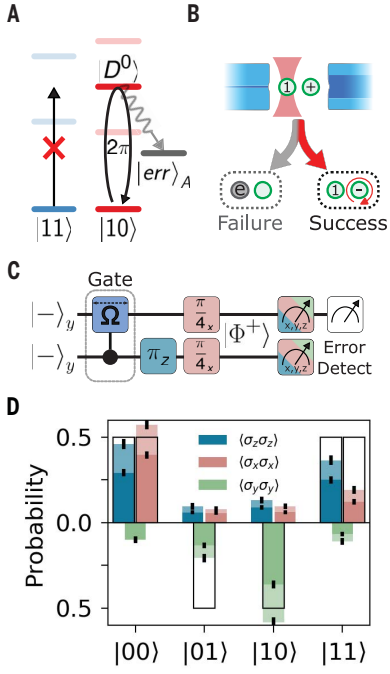

Fig. 4. Deterministic quantum gate with error detection. (**A**) Conditional blockade mechanism. A resonant 2π Rabi oscillation can be realized only between the $|10\rangle$ state and the dark state $|D_0\rangle$, causing a phase of π on state $|10\rangle$, whereas the excitation from the $|11\rangle$ state is blockaded. Unwanted atomic scattering results in mainly detectable $|err\rangle_A$ states. (**B**) Quantum gate flow chart showing the two possible outcomes: "Success" is a conditional phase on atom B, and "Failure" is a detectable scattering event. (**C**) Quantum circuit of the gate. Following the gate, we applied a local Z_π pulse on atom B and a global microwave $X_{\pi/4}$ pulse to generate the $|\Phi^+\rangle$ Bell state. (**D**) Measured correlations in the *ZZ* (blue), *XX* (red), and *YY* (green) bases verify that $|\Phi^+\rangle$ is prepared. Dark shades indicate that without error detection, we measured a deterministic Bell state fidelity of $\mathcal{F} = 52.5(1.8)\%$. Light shades indicate that error detection improves the fidelity to $\mathcal{F}' = 76(2)\%$ with a success probability of 69(1)%. Direction of histograms indicate the expected sign of parity for $|\Phi^+\rangle$ in each base.

rate of entanglement generation and enable faster entanglement preparation [(*29*), section 7.1].

Quantum operations with integrated error detection

The qubit state–dependent resonance can also be used to perform a quantum gate between two atoms. By increasing the strength of the laser, we could drive a coherent optical Rabi oscillation between the $|10\rangle$ state and the photonic dark state $|D_0\rangle$, whereas the $|11\rangle$ state was blockaded from excitation, and both the $|00\rangle$ and $|01\rangle$ states were unaffected by the drive. By performing a full 2π rotation, the $|10\rangle$ would acquire a relative π phase compared with the other three two-qubit states, realizing a controlled phase gate (Fig. 4A). This scheme is limited by scattering; however, most of these events resulted in detectable error states, $|err\rangle_A$, allowing us to increase the fidelity of the measurement through postselection (Fig. 4B).

To characterize the performance of the gate, we prepared an entangled state using the quantum circuit shown in Fig. 4C. For a perfect gate, this circuit would prepare the Bell state $|\Phi^+\rangle = \frac{1}{\sqrt{2}}(|00\rangle + |11\rangle)$. Similar to the carving case, we determined the Bell state fidelity by measuring correlations along all three bases (Fig. 4D). Without any error detection or postselection, the measured Bell state fidelity was $\mathcal{F} = 52.5(1.8)\%$ [(*29*), section 5]. By applying error detection and postselection, we improved the Bell state fidelity to $\mathcal{F}' = 76(2)\%$, with a success probability of 69(1)%. This measurement aligns with the theoretical maximum corrected fidelity of 78% for our cooperativity. The limitation in fidelity is primarily due to the use of atom A as both a qubit and an ancilla to herald the success of the gate. This results in correction creating an imbalance of population between states in which atom A is in $|0\rangle_A$ as opposed to $|1\rangle_A$. Additionally, the states used in the current scheme do not have fully detectable errors and suffer from scattering and a light shift from the $F = 3$ states, resulting in a further reduction in fidelity. These limitations can be addressed in future implementations by including an additional ancillary atom and by more careful selection of atomic states (*29*, *34*, *35*). Such an ancilla could be individually addressed and read out, allowing for the detection of gate errors without affecting the data qubits.

Outlook

Our experiments demonstrated a versatile platform that offers future opportunities by combining neutral-atom arrays with a high-finesse optical cavity. The demonstrated entanglement schemes offer improvements over many existing quantum networking protocols. For example, the probabilistic gate performed by using photon detection, as in (*25*), can be

replaced with cavity carving that includes error detection of the atomic state, potentially increasing the rate of quantum information transmission by at least an order of magnitude. Another extension would be to increase the number of atoms in the cavity, introducing an auxiliary atom to serve as an ancilla for the gate, enhancing gate fidelity (*34*). Moreover, incorporating more qubits would allow for the execution of multiqubit gates (*37*). Higher-fidelity cavity-mediated gates could unlock new possibilities in quantum networking by using many entangled matter qubits, potentially generating many-photon graph states for error-corrected quantum networking protocols (*26*, *38*). Further improvements can be achieved by fabricating higher-quality mirrors to increase cooperativity (*39*, *40*). Combining our platform with Rydberg gate operations in atom arrays would enable fast, high-fidelity, nondestructive midcircuit readout for error-correction protocols and facilitate the entanglement of spatially separated quantum processors for distributed quantum computing, increasing the available number of qubits (*12*, *13*, *15*, *16*). Last, our error-biased mechanism can be extended to more general cavity-mediated interactions, such as long-range spin-spin Hamiltonians and spin squeezing (*41*–*45*).

REFERENCES AND NOTES

1. D. Bluvstein *et al*., *Nature* **626**, 58–65 (2024).
2. I. S. Madjarov *et al*., *Phys. Rev. X* **9**, 041052 (2019).
3. A. W. Young *et al*., *Nature* **588**, 408–413 (2020).
4. A. Cao *et al*., Multi-qubit gates and Schrödinger cat states in an optical clock. arXiv:2402.16289 [quant-ph] (2024).
5. A. L. Shaw *et al*., *Nat. Phys.* **20**, 195–201 (2024).
6. S. J. Evered *et al*., *Nature* **622**, 268–272 (2023).
7. S. Ma *et al*., *Nature* **622**, 279–284 (2023).
8. P. Scholl *et al*., *Nature* **622**, 273–278 (2023).
9. D. Bluvstein *et al*., *Nature* **604**, 451–456 (2022).
10. H. J. Manetsch *et al*., A tweezer array with 6100 highly coherent atomic qubits. arXiv:2403.12021 [quant-ph] (2024).
11. C. Monroe *et al*., *Phys. Rev. A* **89**, 022317 (2014).
12. C. Young *et al*., *Appl. Phys. B* **128**, 151 (2022).
13. W. Huie, S. G. Menon, H. Bernien, J. P. Covey, *Phys. Rev. Res.* **3**, 043154 (2021).
14. P. L. Ocola *et al*., *Phys. Rev. Lett.* **132**, 113601 (2024).
15. Y. Li, J. D. Thompson, *PRX Quantum* **5**, 020363 (2024).
16. J. Sinclair *et al*., Fault-tolerant optical interconnects for neutral-atom arrays. arXiv:2408.08955 [quant-ph] (2024).
17. A. Reiserer, G. Rempe, *Rev. Mod. Phys.* **87**, 1379–1418 (2015).
18. S. Daiss *et al*., *Science* **371**, 614–617 (2021).
19. T. Đorđević *et al*., *Science* **373**, 1511–1514 (2021).
20. Z. Yan *et al*., *Phys. Rev. Lett.* **131**, 253603 (2023).
21. Y. Liu *et al*., *Phys. Rev. Lett.* **130**, 173601 (2023).
22. L. Hartung, M. Seubert, S. Welte, E. Distante, G. Rempe, *Science* **385**, 179–183 (2024).
23. D. Hunger *et al*., *New J. Phys.* **12**, 065038 (2010).
24. R. Gehr *et al*., *Phys. Rev. Lett.* **104**, 203602 (2010).
25. S. Langenfeld, P. Thomas, O. Morin, G. Rempe, *Phys. Rev. Lett.* **126**, 230506 (2021).
26. P. Thomas, L. Ruscio, O. Morin, G. Rempe, *Nature* **629**, 567–572 (2024).
27. S. Singh *et al*., Modular architectures and entanglement schemes for error-corrected distributed quantum computation. arXiv:2408.02837 [quant-ph] (2024).
28. F. Riera Sàbat, W. Dür, *New J. Phys.* **26**, 123015 (2024).
29. Materials and methods are available as supplementary materials.
30. J. Bochmann *et al*., *Phys. Rev. Lett.* **104**, 203601 (2010).
31. M. Martinez-Dorantes *et al*., *Phys. Rev. Lett.* **119**, 180503 (2017).
32. E. Deist *et al*., *Phys. Rev. Lett.* **129**, 203602 (2022).
33. A. Neuzner, M. Körber, O. Morin, S. Ritter, G. Rempe, *Nat. Photonics* **10**, 303–306 (2016).
34. J. Borregaard, P. Kómár, E. M. Kessler, A. S. Sørensen, M. D. Lukin, *Phys. Rev. Lett.* **114**, 110502 (2015).
35. J. Ramette, J. Sinclair, V. Vuletić, Counter-factual carving exponentially improves entangled-state fidelity. arXiv:2401.11407 [quant-ph] (2024).
36. S. Welte, B. Hacker, S. Daiss, S. Ritter, G. Rempe, *Phys. Rev. X* **8**, 011018 (2018).
37. S. Jandura, V. Srivastava, L. Pecorari, G. Brennen, G. Pupillo, Non-local multi-qubit quantum gates via a driven cavity. arXiv:2303.13127 [quant-ph] (2023).
38. J. Borregaard *et al*., *Phys. Rev. X* **10**, 021071 (2020).
39. G. Wachter *et al*., *Light Sci. Appl.* **8**, 37 (2019).
40. N. Jin *et al*., *Optica* **9**, 965–970 (2022).
41. I. D. Leroux, M. H. Schleier-Smith, V. Vuletić, *Phys. Rev. Lett.* **104**, 073602 (2010).
42. K. C. Cox, G. P. Greve, J. M. Weiner, J. K. Thompson, *Phys. Rev. Lett.* **116**, 093602 (2016).
43. C.-L. Hung, A. González-Tudela, J. I. Cirac, H. J. Kimble, *Proc. Natl. Acad. Sci. U.S.A.* **113**, E4946–E4955 (2016).
44. A. Periwal *et al*., *Nature* **600**, 630–635 (2021).
45. M. A. Norcia *et al*., *Science* **361**, 259–262 (2018).

ACKNOWLEDGMENTS

We thank P. Samutpraphoot, T. Đorđević, and P. Ocola for assisting in the early stages of building this experiment; L. Childress, J. Ma, T. Clark, and S. Schwartz for helpful discussion on fiber cavity mounting and alignment; M. Förg and T. Hümmer for useful discussions about fiber cavities; G. Baranes and E. Trapp for insightful discussions; and A. Ruskuc for critical reading of the manuscript. **Funding:** This work was supported by the US Department of Energy (DOE) QSA Center (DE-AC02-05CH11231), the National Science Foundation (NSF) (grant PHY-2012023), the Center for Ultracold Atoms (an NSF Physics Frontiers Center), Army Research Office Multidisciplinary University Research Initiative (W911NF2010082), and Defense Advanced Research Projects Agency Optimization with Noisy Intermediate-Scale Quantum devices (ONISQ) (grant W911NF2010021). The device was fabricated at the Harvard Center for Nanoscale Systems (NSF ECCS-1541959). **Author contributions:** B.G., E.G.-S., and I.D. built the experimental setup, performed the measurements, and analyzed data. D.S. and G.E.M. assisted with experiments. B.G. and J.B. developed the theory for the entanglement schemes. All work was supervised by V.V. and M.D.L. All authors discussed the results and contributed to the manuscript. **Competing interests:** V.V. and M.D.L. are cofounders and shareholders of QuEra Computing. All other authors declare no competing interests. **Data and materials availability:** All data needed to evaluate the conclusions in the paper are present in the paper and the supplementary materials.

SUPPLEMENTARY MATERIALS

science.org/doi/10.1126/science.adr7075
Materials and Methods
Figs. S1 to S10
References (*46*–*50*)

Submitted 7 October 2024; accepted 20 January 2025
10.1126/science.adr7075